INNOVATIVE MECHANICAL ENGINEERING **ISSN 2812-9229 (Online)**
University of Niš, Faculty of Mechanical Engineering
VOL. 1, NO 3, 2022, PP. 39 - 48

Original scientific paper *

THE INFLUENCE OF GEOMETRICAL PARAMETERS ON THE EFFICIENCY OF THE LIQUID JET EJECTOR

Živan Spasić, Veljko Begović, Jasmina Bogdanović Jovanović and Miloš Jovanović

University of Nis, Faculty of Mechanical Engineering, Serbia

Abstract. *Ejectors are jet pumps in which energy to drive fluid is obtained from another fluid. Because they have no moving parts, liquid jet ejectors have found their application in many specific conditions of fluid transport, such as refrigeration, hydraulic transportation, mixing and homogenization of different liquids, changing characteristics of centrifugal pumps, etc. The disadvantage of ejectors is relatively low efficiency. This paper used a method of numerical simulation, the computational fluid dynamics (CFD) method, to study the influence of operating conditions and geometry parameters on the performance of an ejector. This research focuses on the effect of the geometrical and operating parameters of ejectors. Results of a CFD simulation aid the understanding of ejector characteristics and provide information for designing the ejector to suit different entrainment ratios. In addition, they provide a better understanding of the links between geometrical parameters and ejector efficiency. This paper investigates the effects of a few geometrical parameters on the ejector's performance by numerical simulation. The lengths of the primary inlet, secondary inlet, mixing chamber, and diffuser are varied, along with the diameters of the primary and secondary inlet, nozzle, and diffuser. The ANSYS Fluent software package was used for numerical simulations. The primary and secondary fluid is water.*

Key words: *Ejector, Numerical simulations, CFD, ANSYS Fluent, Geometrical parameters, Efficiency*

1. INTRODUCTION

Ejectors are jet pumps in which the second (chased) fluid receives energy to drive from the primary (driving) fluid. Unlike other rotodynamic or positive-displacement pumps, an ejector has no moving parts. There is no rotating impeller or moving element such as a piston. An ejector has four basic components (Fig. 1). The kinetic energy of the high-pressure fluid acts on the low-pressure fluid, causing it to move. The two fluids are mixed in the mixing chamber and carried off to the diffuser, transporting the mixed fluid to the

*Received: December 06, 2022 / Accepted December 27, 2022.
Corresponding author: Veljko Begović
University of Nis, Faculty of Mechanical Engineering, Serbia
E-mail: veljko.begovic@masfak.ni.ac.rs

pipeline. A pressurized liquid functions as a rigid working part and is required to operate jet pumps. In other words, low-pressured water is pumped by high-pressured water, behaving as a driving energy source. Although the water jet pump appears simple concerning its geometry and operation, the negative influence of any error in its design and manufacturing can have a large-scale effect on the pump's efficiency [1]. Ejector design is usually based on a desired working fluid and ejector performance, which is sensitive and depends on the operating conditions. It should be noted that the performance of ejectors is strongly correlated to their geometry and flow characteristics because ejectors are characterized by complex fluid dynamics at the "local scale" [2]. Indeed, a well-designed ejector could only operate effectively when the operating conditions approach the design conditions [3].

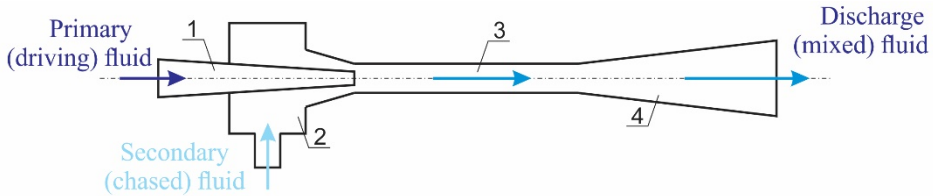

Fig. 1 Schematic view of liquid ejector elements: nozzle (1), suction chamber (2), mixing chamber (3) and diffuser (4).

The main disadvantage of ejectors is relatively low efficiency; the low energy efficiency of ejectors is caused by friction losses and the fluid mixing process [4]. Many methods have been adopted to improve ejector performance, such as ejector geometrical parameter optimisation and adjustable ejector structure. In general, the ejector performance is closely related to its structural factors, so many investigators do their best to obtain the optimal ejector structural parameters for the maximum entrainment ratio. Paper [5] showed how changing the area of the ejector can affect the performance and increase the efficiency from 0.29 to 0.41. The ejector performance is very sensitive to the mixing tube length. At the same time, the entrainment ratio can vary up to 27% by changing the mixing tube length [6]; in contrast, [7] pointed out that the entrainment ratio was almost independent of the mixing tube length. In [8] the authors concluded that normalised mixing tube length (L_{mix}/D_{mix}) of 7–9, the area ratio of 0.28 and a modified shape of the outer wall of the driving nozzle, can increase efficiency up to 40%. The influence of various geometrical factors on the ejector performance is coupled. In order to achieve optimal geometrical parameters, it is necessary to optimise its overall geometrical shape [9]. A lot of different geometries were analysed using numerical simulations. Nine different geometries were selected and will be presented in what follows.

2. EJECTOR GEOMETRY

The ejector geometry shown in Fig. 2 was built as the base for the initial simulations. For the base geometry, an ejector of known geometry was selected. For this base geometry, the curves that limit the suction chamber and primary inlet are spline curves. The rest of the boundaries are straight lines. For numerical simulations, the axisymmetric geometry of

the ejector was adopted. The use of axisymmetric geometry allows for reducing the required computing resources and the generation of a finer mesh.

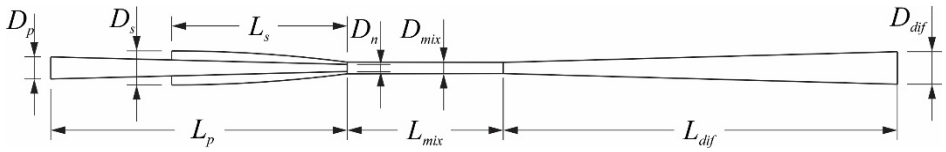

Fig. 2 Ejector base geometry

The corresponding geometrical parameters for the base ejector, symbols, and values are presented in Table 1.

Table 1 Geometrical parameters of the ejector

Geometrical parameter	Symbol	Value [mm]
Diameter of the primary inlet	D_p	11.26
Diameter of the secondary inlet	D_s	17.36
Diameter of the nozzle	D_n	3.61
Diameter of the mixing chamber (throat)	D_{mix}	5.94
Diameter of the diffuser	D_{dif}	16.58
Length of the primary nozzle inlet	L_p	152
Length of the secondary inlet	L_s	90
Length of the mixing chamber	L_{mix}	80
Length of the diffuser	L_{dif}	200

In order to analyze the influence of certain geometrical parameters on ejector performance, the following modifications have been made to the ejector geometry. The lengths of the primary inlet, secondary inlet, mixing chamber, and diffuser were changed along with the diameters of the primary and secondary inlet, nozzle, and diffuser. Of the many cases, nine of the more interesting ones were chosen and presented.

Geometrical changes that were made are given below. In case 1 the length of the primary nozzle inlet (L_p) was changed to 120 mm, in case 2, the length of the primary nozzle (L_p) remained as in case 1, the primary inlet diameter (D_p) was changed to 13.78 mm and the diameter of the nozzle (D_n) was increased to 3.8 mm, and in case 3, the values of L_p and D_p remained as in the previous case, while the diameter of the nozzle (D_n) was changed to 2.8 mm. In case 4, in addition to L_p and D_p, as in the previous two cases, the diameter of the mixing chamber (D_{mix}) was changed to 6.4 mm. In case 5, the length of the mixing chamber (L_{mix}) was set to 100 mm and the length of the diffuser (L_{dif}) to 180 mm. In cases 6 and 7, the mixture chamber length was changed to 50 and 60 mm, respectively. In case 8 the mixing chamber length (L_{mix}) was reduced to 50 mm and the diameter of the diffuser outlet (D_{dif}) to 20 mm. Case 9 included and unified positive findings from all previous cases. The length of the mixing chamber (L_{mix}) was set to 50 mm, the length of the primary nozzle inlet (L_p) to 120 mm, and the diffuser outlet diameter (D_{dif}) to 20 mm.

3. EJECTOR EFFICIENCY

The efficiency and pressure lift for an incompressible fluid ejector can be written respectively as [10]:

$$\eta = M \cdot N \tag{1}$$

$$N = \frac{P_d - P_s}{P_p - P_d} \tag{2}$$

where:

- M – entrainment ratio defined by $M = Q_s / Q_p$,
- Q_s – volumetric flow ratio of the secondary fluid (suction chamber flow),
- Q_p – volumetric flow ratio of the primary fluid (nozzle flow),
- N – pressure ratio,
- P_d – total pressure at the diffuser outlet,
- P_s – total pressure at the suction chamber inlet,
- P_p – total pressure at the primary inlet.

4. CFD MODELING

This work presents CFD simulations performed in the commercial software package ANSYS Fluent (version 22R1). Fluent is used for 3D fluid flow analysis, describing fluid flow using mass, momentum, and energy conservation equations. Ansys Fluent solves Reynolds-Averaged Navier Stokes (RANS) equations using a finite volume discretization method over the partial differential equations that govern the fluid flow.

The continuity equation:

$$\frac{\partial \rho}{\partial t} + \frac{\partial}{\partial x_i}\left(\rho u_i\right) = 0 \tag{3}$$

The momentum equation:

$$\frac{\partial}{\partial t}\left(\rho u_i\right) + \frac{\partial}{\partial x_j}\left(\rho u_i u_j\right) = -\frac{\partial p}{\partial x_i} + \frac{\partial}{\partial x_j}\left[\mu\left(\frac{\partial u_i}{\partial x_j} + \frac{\partial u_j}{\partial x_i} - \frac{2}{3}\delta_{ij}\frac{\partial u_i}{\partial xi}\right)\right] + \frac{\partial}{\partial x_j}\left(-\rho\overline{u_i' u_j'}\right) \tag{4}$$

Where the Reynolds stresses are defined by the expression:

$$-\rho\overline{u_i' u_j'} = \mu_t\left(\frac{\partial u_i}{\partial x_j} + \frac{\partial u_j}{\partial x_i}\right) - \frac{2}{3}\left(\rho k + \mu_t \frac{\partial u_k}{\partial x_k}\right)\delta_{ij} \tag{5}$$

4.1. Turbulent model

Four turbulent models were tested: $k-\varepsilon$ standard, $k-\varepsilon$ realizable, $k-\omega$ and $k-\omega$ SST. The mentioned turbulence models have performed well in complex geometries, multiphase flows, channels, mixing and separated flows, etc. The analysis and validation of these

turbulence models can be found in many different studies in the literature. In [11] the authors used *k-ε* standard which estimated the efficiency at 34.9%. The authors in [12] analysed *k-ε*, *k-ω* and *k-ω* SST turbulence models. It was concluded that the model *k-ω* SST gives the best results and matches the experimental values, while *k-ω* was rejected due to a significant deviation. On the other hand, in paper [13] it is the *k-ω* SST model that showed the best performance for different operating conditions and geometries studied. In this research, it was decided to use the *k-ω* SST turbulent model based on the conclusions from the literature and comparison (Fig. 3) of turbulence models.

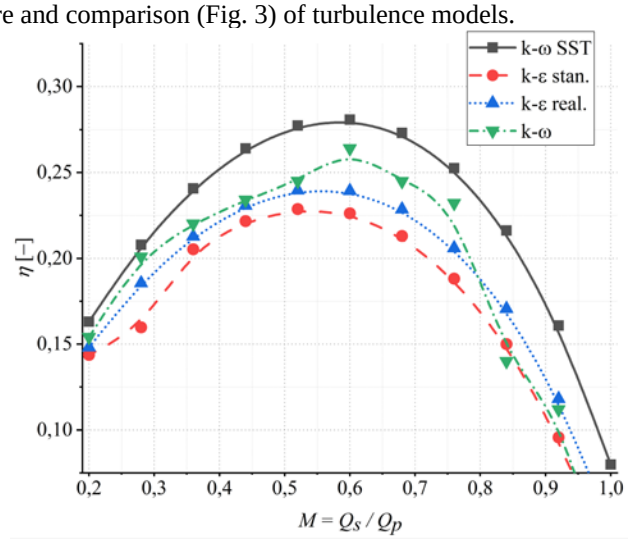

Fig. 3 Ejector efficiency (η) as a function of the entrainment ratio - comparison of different turbulent models (M)

The SST *k-ω* is a two-equation turbulence model. It is a hybrid model combining the Wilcox *k-ω* and the *k-ε* models. The blending function is designed to be one in the near-wall region, which activates the standard *k-ω* model, and the *k-ε* model in the free stream. The *k-ω* SST model guarantees that the suitable model is used throughout the flow field. The *k-ω* model is well suited for simulating flow in the viscous sub-layer and the *k-ε* model is ideal for predicting flow behaviour in regions away from the wall. The SST *k-ω* model is determined by the following transport equations, in which *k* represents the turbulent kinetic energy, while *ω* represents the vorticity:

$$\frac{\partial}{\partial t}(\rho k)+\frac{\partial}{\partial x_i}(\rho k u_i)=\frac{\partial}{\partial x_j}\left(\Gamma_k \frac{\partial k}{\partial x_j}\right)+\bar{G}_k-Y_k+S_k \tag{6}$$

$$\frac{\partial}{\partial t}(\rho \omega)+\frac{\partial}{\partial x_i}(\rho \omega u_i)=\frac{\partial}{\partial x_j}\left(\Gamma_\omega \frac{\partial \omega}{\partial x_j}\right)+G_\omega-Y_\omega+D_\omega+S_\omega \tag{7}$$

In these equations, $\bar{G}_k$ represents the generation of turbulent kinetic energy due to mean velocity gradients. G_ω represents the generation of the vorticity ω. Γ_k and Γ_ω

represents the effective diffusivity of k and ω, respectively, which are calculated as described below. Y_k and Y_ω represent the dissipation of k and ω due to turbulence. D_ω represents the cross-diffusion term, calculated as described below. S_k and S_ω are user-defined source terms [14].

The effective diffusivities are defined by the following equations:

$$\Gamma_k = \mu + \frac{\mu_t}{\sigma_k}; \qquad \Gamma_\omega = \mu + \frac{\mu_t}{\sigma_\omega} \tag{8, 9}$$

where σ_k and σ_ω are the turbulent Prandtl numbers. The turbulent viscosity (kinematic eddy viscosity) μ_t, is calculated as follows:

$$\mu_t = \frac{\rho k}{\omega} \frac{1}{\max\left[\frac{1}{\alpha^*}, \frac{SF_2}{\alpha_1 \omega}\right]} \tag{10}$$

Where S represents the strain rate magnitude, coefficient α^* damps the turbulent viscosity causing a low-Reynolds-number correction, and F_2 represents the blending function.

The term $\tilde{G}_k$ is used to describe the production of turbulence kinetic energy and G_ω represents the production of vorticity ω, defined by:

$$\tilde{G}_k = \min\left(G_k, 10\rho\beta^* k\omega\right); \qquad G_\omega = \frac{\alpha}{\mu_t}\tilde{G}_k \tag{11}$$

The terms Y_k and Y_ω represent the dissipation of k and ω, respectively, and are defined as follows:

$$Y_k = \rho\beta^* k\omega; \qquad Y_\omega = \rho\beta\omega^2 \tag{12}$$

The introduction of the cross-diffusion term D_ω defined by ω and k is necessary because it represents the connection between k-ω and the k-ε models. D_ω is defined as:

$$D_\omega = 2\left(1 - F_1\right)\rho\sigma_{\omega,2}\frac{1}{\omega}\frac{\partial k}{\partial x_j}\frac{\partial \omega}{\partial x_j} \tag{13}$$

The constants are displayed as follows: $\sigma_{k,1} = 1.176$, $\sigma_{\omega,1} = 2.0$, $\sigma_{k,2} = 1.0$, $\sigma_{\omega,2} = 1.168$, $\alpha_1 = 0.31$, $\beta_{i,1} = 0.075$, $\beta_{i,2} = 0.0828$.

4.2 Boundary conditions

The boundary conditions used in the numerical simulations are presented in Table 2. The solver type is *pressure-based* and uses a solution algorithm where the governing equations are solved sequentially. For discretization a *coupled* scheme was used. The convergence criteria for continuity, momentum, and transport (model) equations were always less than 10^{-7}.

Table 2 Boundary conditions

Boundary	Condition
Nozzle inlet (primary inlet)	Mass flow equals to 0.25 kg/s (Q_p=0.25·10^{-3} m^3/s)
Suction chamber inlet (secondary inlet)	Mass flow (as the function of M)
Diffuser outlet	Static pressure equals to 0.68 – 1.68·10^5 Pa
Walls	No slip conditions
Axis	Axisymmetric

4.3 Mesh analysis

Three different mesh sizes were tested to assess convergence and mesh independence. They were composed of quadrilateral elements with a face meshing option for controlling the number of elements. The simulation results for the ejector efficiency are shown in Fig. 4, correlated to the mesh size. The analysed meshes were: Coarse (2938 elements), Normal (11720 elements) and Fine (46880 elements). As expected, the mesh that gave the best results convergence was the "fine" mesh (Fig. 5), which was the mesh used in the further simulations of this study.

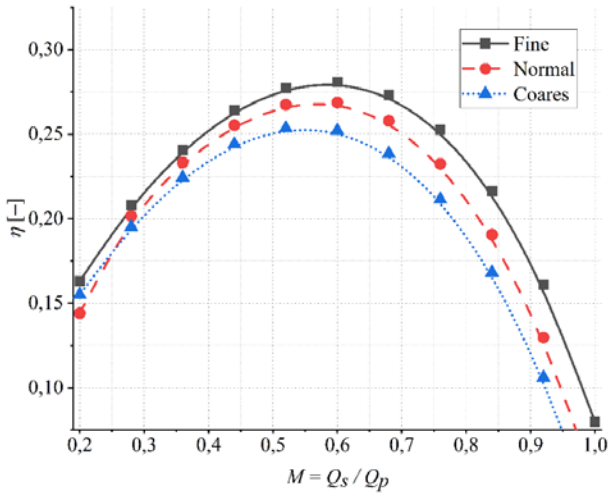

Fig. 4 Comparing meshes with different numbers of elements

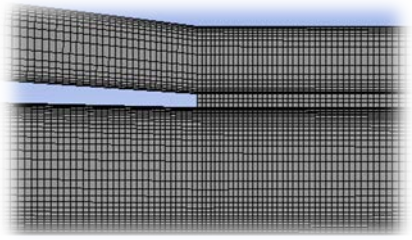

Fig. 5 Detail of the "fine" mesh

5. RESULTS

In the first four cases, ejector efficiency (η) as a function of the entrainment ratio (M) is shown in Fig. 6, while that same dependence for cases 5 to 9 is shown in Fig. 7.

For the first four cases, the length of the primary inlet (L_p) was reduced to 120 mm. This resulted in a slight increase in the secondary inlet diameter (D_s), but care was taken not to change the cross-section area. In cases 2-4, the diameter of the primary inlet (D_p) was reduced. In the first case, there was a slight increase in efficiency. In the second case, the diameter of the nozzle (D_n) was increased to 3.8 mm, while in the third case, it was reduced to 2.8 mm. It can be noticed that with the change in the nozzle diameter, the entrainment ratio changed. The entrainment ratio increased with a decrease in the diameter, and with an increase in the diameter, it decreased. In both cases, it deviated from the assigned entrainment ratio of 0.6. The fourth case contained the same changes as the third because the diameter of the mixing chamber was increased to 6.4 mm, and the maximum efficiency rose to 0.32, but for an entrainment ratio of 0.76. All modified geometrical parameters for cases 1 to 4 are given in Table 3.

Table 3 Modified geometrical parameters for the ejector for cases 1 to 4.

Cases	Geometry changes, [mm]		
Case 1	L_p = 120		
Case 2	L_p = 120	D_p = 13.78	D_n = 3.8
Case 3	L_p = 120	D_p = 13.78	D_n = 2.8
Case 4	L_p = 120	D_p = 13.78	D_{mix} = 6.4

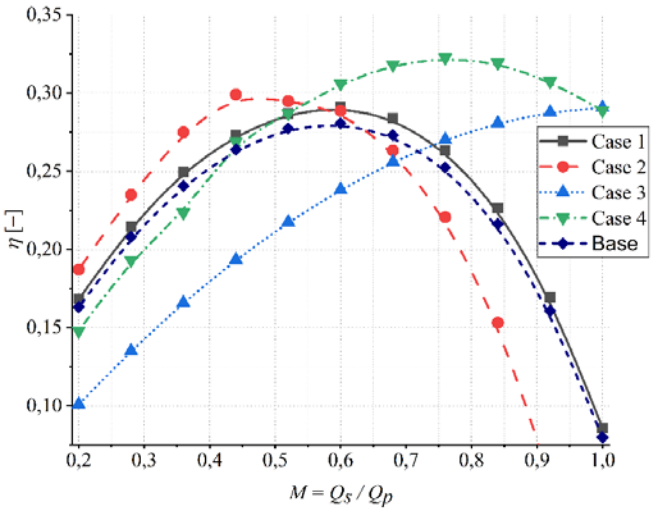

Fig. 6 Ejector efficiency *(η)* as a function of the entrainment ratio *(M)* for cases 1 to 4

It was observed that increasing the length of the mixing chamber (L_{mix}) did not improve efficiency (case 5). In cases 6 and 7, the mixing chamber (L_{mix}) length was restricted to 60 and 50 mm, respectively, favouring efficiency. In case 8, in addition to shortening the

mixing chamber (L_{mix}) to 50 mm, the diameter of the outlet diffuser (D_{dif}) was increased to 20 mm, which again had a beneficial effect on the efficiency of the ejector. The last case considered in this study (case 9) was a combination of favourable geometry changes, which were reached in earlier considerations. In addition to reducing the mixing chamber length and increasing the diffuser's diameter, the primary inlet (L_p) length was reduced to 120 mm. It gave the most favourable effect on efficiency, which grew to 0.328. It should be noted that changing the parameters in cases 5 to 9 did not change the position of the maximum efficiency as a function of the entrainment ratio. All modified geometrical parameters for cases 5 to 9 are given in Table 4.

Table 4 Modified geometrical parameters for the ejector for cases 5 to 9

Cases	Geometry changes, [mm]		
Case 5	L_{mix} = 100		L_{dif} = 180
Case 6	L_{mix} = 60		
Case 7	L_{mix} = 50		
Case 8	L_{mix} = 50		D_{dif} = 20
Case 9	L_{mix} = 50	L_p = 120	D_{dif} = 20

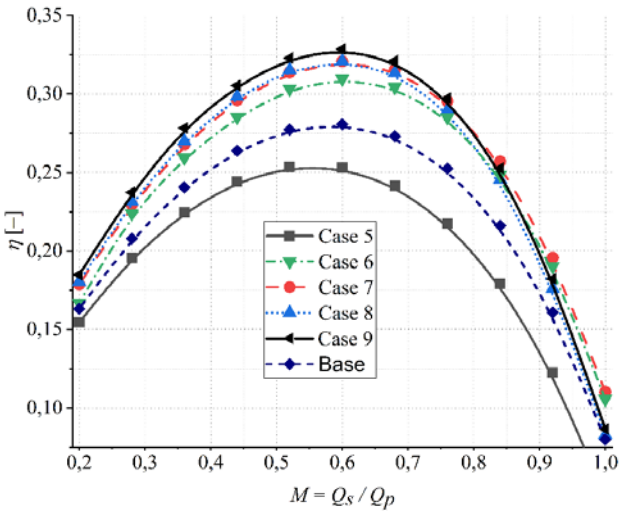

Fig. 7 Ejector efficiency *(η)* as a function of the entrainment ratio *(M)* for cases 5 to 9

5. Conclusions

This study presented the numerical simulations (CFD) of the flow in the ejector and the results of nine different geometries of water ejectors. After the reported analysis and comparison of four turbulent models, the choice came down to the *k-ω* SST turbulent model. The improvement of the performance was based on changing the geometrical parameters of the ejector, and the most significant results are presented in the paper.

It can be noted that the most significant effect on improving the degree of usefulness was achieved by reducing the length of the mixing chamber. A slightly smaller effect was achieved by reducing the length of the inlet chamber and increasing the diameter of the diffuser. Case 9 displayed the highest efficiency improvement of 17.1% over the base geometry. Changing the nozzle diameter causes a change in the position of the maximum efficiency as a function of the entrainment ratio. In further research, the authors will focus on the nozzle geometry influence on the ejector efficiency, as well as on the experimental investigations of the flow in the ejector and validation of the presented numerical results.

Acknowledgement: *This research was financially supported by the Ministry of Education, Science and Technological Development of the Republic of Serbia (Contract No. 451-03-9/2021-14/200109).*

REFERENCES

1. Yapıcı R., Aldaş K., 2013, *Optimization of water jet pumps using numerical simulation*, Journal of Power and Energy, 227(4), pp. 438–449.
2. Besagni G., 2019, *Ejectors on the cutting edge: The past, the present and the perspective*, Energy, 170, 998–1003.
3. Chen W., Chen H., Shi C., Xue K., Chong D., Yan J., 2016, *A novel ejector with a bypass to enhance the performance*, Applied Thermal Engineering, 93, pp. 939–946.
4. Zhang H., Wang L., Jia L., Wang H., 2018, *Assessment and prediction of component efficiencies in supersonic ejector with friction losses*, Applied Thermal Engineering, 129, pp. 618-627.
5. Yapıcıa R., Ersoya H.K., Aktoprakoğlua A., Halkacıa H.S., Yiğitb O., 2018, *Experimental determination of the optimum performance of ejector refrigeration system depending on ejector area ratio*, International Journal of Refrigeration, 33(7), pp. 1183-1189.
6. Maghsoodi A., Afshari E., Ahmadikia H., 2014, *Optimization of geometric parameters for design a high-performance ejector in the proton exchange membrane fuel cell system using artificial neural network and genetic algorithm*, Applied Thermal Engineering, 71(1), pp 410-418.
7. Pianthong K., Seehanam W., Behnia M., 2007, *Investigation and improvement of ejector refrigeration system using computational fluid dynamics technique*, Energ Convers Manage, 48(9), pp. 2556–2564.
8. Mallela R., Chatterjee D., 2011, Numerical investigation of the effect of geometry on the performance of a jet pump, Journal of Mechanical Engineering Science, 225, pp. 1614 – 1625.
9. Samsam-Khayani H., Park S.H., Ha M.Y., Kim K.C., 2022, *Design modification of two-dimensional supersonic ejector via the adjoint method*, Applied Thermal Engineering, 200, 117674.
10. Winoto S. H., Li H., Shah D. A., 2000, *Efficiency of jet pumps*, Journal of Hydraulic Engineering, 126(2), pp. 150–156.
11. Long X., Han N., Chen Q., 2008, *Influence of nozzle exit tip thickness on the performance and flow field of jet pump*, Journal of Mechanical Science and Technology, 22 (11) pp. 1959–1965.
12. Besagni G., Mereu R., Inzoli F., Chiesa P., 2017, *Application of an integrated lumped parameter-CFD approach to evaluate the ejector-driven anode recirculation in a PEM fuel cell system*, Applied Thermal Engineering, 121, pp. 628–651.
13. de Oliveira Marum V.J., Reis L.B., Maffei F.S., Ranjbarzadeh S., Korkischko I., dos Santos Gioria R., Meneghini J.R., 2021, *Performance analysis of a water ejector using Computational Fluid Dynamics (CFD) simulations and mathematical modeling*, Energy, 220, 119779.
14. Fluent Inc., 2009, *Fluent 12.0 User's Guide*, ANSYS Inc, USA, Canonsburg.